Bounding transverse permeability of fibrous media: a statistical study from random representative volume elements with consideration of fluid slip

Aubin Geoffre, Maydine Ghestin, Nicolas Moulin, Julien Bruchon, Sylvain Drapier

Bounding transverse permeability of fibrous media: a statistical study from random representative volume elements with consideration of fluid slip

Aubin Geoffre[a,*], Maydine Ghestin[a], Nicolas Moulin[b], Julien Bruchon[b], Sylvain Drapier[b]

[a] *Industrial Chair Hexcel - Mines Saint-Étienne, Université de Lyon, CNRS, UMR 5307 LGF, Centre SMS*
158 Cours Fauriel - 42023 Saint-Étienne, France
[b] *Mines Saint-Étienne, Université de Lyon, CNRS, UMR 5307 LGF, Centre SMS*
158 Cours Fauriel - 42023 Saint-Étienne, France

Abstract

In this article, a statistical study on transverse permeability of random fibrous medium is performed. For that purpose, numerous random numerical microstructures are generated with constant or randomly varying fibre radii. Their statistical representativity with respect to experimental data is first briefly discussed. Flow simulations are then performed on these digital microstructures to retrieve their full transverse permeability tensor. The representative volume element (RVE) size is determined by studying convergence of permeability distribution when domain size increases. This allows to characterise the medium isotropy as well as the impact of geometrical randomness on permeability. The approach also integrates Gaussian process regression, that is a Bayesian machine-learning model, to consider variability within interpolation in the proposed permeability predictive model. In addition, this paper considers the impact of fluid slip at liquid/fibre interface on permeability for random fibrous media. An analytical expression is proposed to describe precisely the transition from a no-slip to a free-slip regime. This allows us to propose a probabilistic model that links permeability to both the fibre volume ratio and slip length. This finally yields two bounds for transverse permeability of fibrous media: a first related to statistical scattering and a second purely linked to fluid slip.

Keywords: Numerical permeability, Statistics, Fluid slip, Gaussian process regression

1. Introduction

Permeability is a key notion for describing flows within porous materials. As a consequence, this tensorial characteristic has been extensively studied in numerous scientific communities [21, 82] including modelling of manufacturing processes such as Liquid Composite Moulding (LCM) for long carbon fibre reinforced polymers wherein a viscous fluid impregnates fibrous preforms [13, 30, 62, 76].

Classically, flows in porous media can be studied at various scales. Experimental approaches to describe permeability of fibrous materials operate at a macroscopic scale (i.e. the laboratory scale). They were found to suffer from a lack of reproducibility as well as a high sensitivity to laboratories settings [5, 79]. On the contrary, analytical and computational approaches consist in local studies of flows across fibrous microstructures. Both local and macroscopic descriptions can be connected through an upscaling procedure from which permeability naturally shows up. Considering local scale approaches, analytical models that are convenient to use [11, 14, 29] lean on geometrical simplifications that do not allow to consider realistic systems with intrinsic variabilities (e.g. random fibre radius, random fibre placement,...) as observed in manufacturing processes. These limitations lead researchers to develop numerical strategies to characterise permeability more accurately [2, 20, 58]. This approach first requires virtual geometries. Those can be obtained from digitisation of real-world materials thanks to recent tomography techniques [3, 89] or in a pure numerical way with textile modelling software [26, 50] or random non-overlapping disk algorithms. The latter will be detailed in Section 2.1. This work is primarily oriented towards modelling the manufacturing processes of composite materials, although these results can be relevant wherever a viscous flow in a fibrous medium is observed: textile, biomechanics,... In this study, no direct comparison with experimental permeability measurements will be carried out. However, comparisons with other numerical results — which has been found to be consistent with the experiment — will be performed.

From those fibrous geometries, mass (Eq.1) and momentum (Eq.2) local conservation equations for a newtonian incompressible viscous fluid (i.e. Stokes equations) are classi-

*Corresponding author
Email address: a.geoffre@emse.fr (Aubin Geoffre)

cally solved to first represent the fluid flow across the fibrous arrangements and then to assess their permeability. This is done through various numerical methods: Finite Element Method (FEM) [73], Lattice Boltzman Method (LBM) [35], Fast Fourier Transform (FFT) [1, 83],...

$$\boldsymbol{\nabla} \cdot \boldsymbol{v} = 0 \tag{1}$$

$$\mu \boldsymbol{\Delta} \boldsymbol{v} - \boldsymbol{\nabla} p = \mathbf{0} \tag{2}$$

where $\boldsymbol{v}$ is the fluid velocity, p the fluid pressure and μ the fluid viscosity. As indicated previously, those local equations can be upscaled to get a macroscopic description of the fluid flow within the porous structure. This corresponds to Darcy law [6, 21, 82]:

$$\boldsymbol{\nabla} \cdot \boldsymbol{v}_D = 0 \tag{3}$$

$$\boldsymbol{v}_D = -\frac{1}{\mu} \boldsymbol{K} \cdot \boldsymbol{\nabla} p_D \tag{4}$$

where $\boldsymbol{v}_D$ (resp. p_D) is the upscaled velocity (resp. pressure) and $\boldsymbol{K}$ the second-order permeability tensor. This permeability term naturally comes from the upscaling procedure: it encompasses all the effects leading to the fluid energy loss, i.e. fluid viscosity effects and its contact with fibres [82]. Hence both contributions of flow channels formed between fibres and fluid/fibres interaction should be investigated. It has been also highlighted that permeability may be affected by thermal effects or by the type of fluid under consideration [70]: those contributions will be neglected here. In practice, solution fields at the local scale are integrated to then compute permeability from Eq.4 (Section 2.3). Permeability tensor $\boldsymbol{K}$ is generally represented by a diagonal matrix since fluid is assumed to flow along the principal directions of the medium under consideration. This assumption is however rarely verified [56] as computing off-diagonal components of the permeability tensor may be challenging. In this paper, geometrical periodicity allows to provide periodic boundary conditions leading to a direct computation of the off-diagonal components. The importance of those terms will be discussed.

That upscaling procedure must be performed on a representative volume element (RVE) that is the smallest geometry for which permeability becomes independent of the

domain size [9, 32, 33, 36, 72, 75]. Numerical permeability of fibrous media is then generally studied from single deterministic unit cells that are supposed to be representative of real-world materials [30, 60]. Yet, fibrous materials display a natural geometrical complexity that justifies a statistical modelling [17, 86, 87, 90]. As a consequence, for a given fibre volume fraction V_f value, permeability tensor of numerous random RVEs should be computed to provide an accurate characterisation of the property. This is done in this paper where the tensors computed from microstructures are regarded as realisations of a permeability continuous random variable. Only few papers can be found with a similar methodology for permeability study of fibrous materials [8, 90]. This approach differs from [74, 75] where a statistical RVE (SRVE) is defined as a geometry sufficiently large to capture both physical and geometrical information.

As noticed previously, permeability can be related to fluid/fibres interaction. As a consequence, the condition provided at the liquid/solid interface has a direct impact on the permeability. As carbon fibre radius is around 3.3 μm [77] and industrial requirements for V_f may be close to 0.6, flow channels between fibres may become submicrometric. At this scale, the usual no-slip condition at the liquid/solid interface should be reconsidered to take fluid slip into account [59, 71, 91]. Fluid slip is an active research topic in various communities [16, 46, 47, 66, 68]. It can be explained by surface roughness effects as well as chemical fluid/solid affinity [41]. This is in line with industrial observations according to which permeability measurements may be sensitive to carbon fibres surface treatment [25]. Fluid slip consideration is also convenient when it comes to modelling moving fluid front in transient multiphase flows as it allows to alleviate Huh-Scriven paradox [39]. Details on fluid slip origins and terminologies can be found in [81].

Mathematically, fluid slip is generally expressed through Navier slip condition [57] at the liquid/solid interface Γ_{LS}. It relates tangential fluid velocity to shear components of fluid Cauchy stress tensor $\boldsymbol{\sigma}$ (Fig.1):

$$\boldsymbol{v} \cdot \boldsymbol{t} = -\frac{\ell_s}{\mu} \boldsymbol{t} \cdot \boldsymbol{\sigma} \cdot \boldsymbol{n} \quad \text{on } \Gamma_{LS} \tag{5}$$

where ℓ_s is the slip length, and $\boldsymbol{t}$ (resp. $\boldsymbol{n}$) is a unit tangential (resp. normal) vector to Γ_{LS}. This generalises no-slip ($\ell_s \to 0$) and free-slip conditions ($\ell_s \to \infty$) [78, 80]. Many articles can be found on experimental or numerical determination of slip length for various fluid/solid couples [42, 43, 63]. It is generally found to span from $10^{-9}m$

to $10^{-6}m$. Maali *et al.* [51] estimate the slip length for water/graphite couple to be 8 ± 2 nm. It can be then remarked that those orders of magnitude can be comparable to the characteristic size of flow channels within our microstructures. Slip length will be considered here as a constant parameter even if its dependencies to other characteristics of the flow might be complex and still on study [4, 41, 52, 66]. However, as slip length mainly acts as an intrinsic property of the fluid/solid couple, it seems appropriate to consider it as independent of the imposed pressure drop — at least for a newtonian fluid. The influence of slip length value on permeability of idealised geometries has been investigated in few articles [7, 27, 28, 45]. One of the novelties of this paper is to consider fluid slip on numerous RVEs of fibrous media on top of other sources of variability.

We will first describe the microstructure generation method and its representativity (Section 2.1). Full permeability tensor (Section 2.3) of numerous generated geometries will be then computed from finite element solving (Section 2.2) of Stokes equation. This will allow to determine the domain size to reach a RVE (Section 3.1). Then isotropy of the RVEs will be discussed (Section 3.2). The influence of fibres centre randomness (Section 3.3) and radius variability (Section 3.4) on permeability will be also detailed. Gaussian process regression (Section 2.4) will be integrated into the statistical analysis. In the end, fluid slip will be considered and its influence on permeability will be characterised (Section 3.5). A probabilistic model that links permeability to V_f and slip length will be finally proposed. This will give boundings to stochastic permeability. Those results will be then discussed (Section 4): comments will be first made about the variability of permeability. Then the influence of fluid slip on permeability — with slip lengths consistent with available experimental measurements — will be discussed.

2. Materials and methods

2.1. Microstructure generation algorithm and representativity

Various numerical methods for microstructure generation can be found in the literature [55, 84, 85]. Those consist in non-overlapping disk placement methods that are finally supposed to be representative of the transverse section of long fibre composite materials. The most straightforward algorithm is named hard-core method and consists in placing fibre centers totally randomly before performing a non-overlapping test of

2D cross-sections [12]. This method is highly limited by jamming effect that prevents from reaching high V_f. The algorithm can be adapted to reduce this effect and provide geometrical periodicity [55].

Another technique consists in starting from an initial configuration that is subsequently perturbated randomly by picking a random displacement vector for each fibre [15, 34, 84]. Potential-based methods that consider fibres as a set of interacting particles seem to be the most efficient to reach high V_f [40, 49]. In spite of the efficiency of the presented algorithms, the question of representativity still remains. This is regularly assessed through Complete Spatial Randomness (CSR) characterisation thanks to related tools such as Ripley's function [65]. However, such a consideration does not lie on experimental observations. In addition, total randomness cannot be observed at high V_f due to the non-overlapping condition. Indeed, it entails forbidden positions for fibre placement that result in a biased CSR: this is comparable to an interaction potential between fibres [8, 31, 33]. To overcome this issue, generation algorithms that are directly based on experimental parameters distribution can be also proposed [77]. Despite the representativity of these approaches, it has been finally shown in [87] that fibrous geometries and permeability results slightly depend on generation algorithm, at least for moderate V_f values. At last, only few algorithms take radius randomness into account [49, 54] while it may entail an additional source of variability. Its influence will be investigated in this paper.

In the context of this study, the requirements related to the generation method were multiple. First, the algorithm should reach V_f values around 0.6 to be relevant for industrial applications. Then the generated microstructures should display a variability C_r of fibre radius r that is set at 10% in this work. Fibre radius should follow a normal distribution: $r \sim \mathcal{N}(\bar{r}, C_r\bar{r}) = \mathcal{N}(\bar{r}, 0.1\bar{r})$. The microstructures should also be periodical to provide periodic boundary conditions. Indeed, this allows to be consistent with rigourous homogeneisation procedures and to reach a RVE for smaller domain size since edge effects are prevented [88]. At last, the method should be computationnally efficient enough to generate numerous microstructures.

For all these reasons, this work focus on a simple method that generates microstructures within a square domain of size L^2 by perturbating an initally dense quadratic

packing (Fig.2). It is based on an algorithm proposed in [34] with some differences. Fibre centres are first placed according to a quadratic packing of maximum compacity. Then random radii are picked in a Gaussian law $\mathcal{N}(\bar{r}, C_r\bar{r})$ and a non-overlapping condition is enforced. The value of $\bar{r}$ can be directly computed from both domain size and V_f:

$$\bar{r} = L\sqrt{\frac{V_f}{N\pi}} \tag{6}$$

where N is the number of fibre contained inside the domain that is explicitly calculated from V_f and L considering a quadratic packing. Then a random displacement vector is applied on each fibre. This displacement is kept if it does not lead to fibre overlapping or to a distance between fibres so small that it could cause mesh refinement issues: it is here chosen to reject distances inferior to $0.07\bar{r}$. This is repeated N_p times. That step also provides geometrical periodicity as a fibre going out of the domain reenters on the opposite side. The algorithm is also convenient to generate microstructures with a constant fibre radius by taking $C_r \ll 1$. An example of numerically generated microstructure with varying radius can be observed in Fig.3.

Other generation algorithms have also been tested. It has been remarked that the targeted fibre radius variance could be difficult to retrieve, especially for high V_f values. This is directly related to the non-overlapping rejecting test. The generation algorithm described previously has been found to be suitable to limit this problem. Indeed, for all the V_f considered here, a Gaussian radius variability with $C_r \sim 10\%$ can be retrieved. Through this algorithm, the obtained V_f value may slightly differ from the targetedone, especially for $V_f > 0.55$. Indeed, a limit is observed for $V_f \sim 0.62$: higher V_f values cannot be reached. Even if the maximum compacity for a quadratic packing is close to 0.78, a compromise between obtaining very high V_f values and mesh issues has to be achieved. Indeed, for very high V_f values, flow channels become so narrow that ensuring a sufficient number of finite elements to represent the flow profile correctly may be complex. It should be remarked that this issue could be alleviated by using anisotropic mesh adaptation techniques [23] that would help to reach higher V_f values.

Representativity of the generated microstructures should be next assessed. The CSR criterion is here rejected due to the arguments developed previously : the non-overlapping condition makes irrelevant complete spatial randomness as it acts as an interaction po-

tential between fibres. We choose to compare first and second nearest neighbour (NN) distance distributions of the generated microstructures to experimental ones. Further microstructural parameters are commonly used in literature : Delaunay triangulation [87], Voronoi tesselation characteristics [67],... However, first and second NN distances are one of the most straightforward tools to characterise fibrous microstructures on a first approach. These morphological parameters measure short-range interactions of the particules.

Experimental microstructure analyses are so rare that we struggled to find some well described data for comparing with our virtual microstructures. In Fig.4, we compared our NN distributions to results from Vaughan and McCarthy [77] that consider experimental distributions of carbon fibres for high performance composite materials with high V_f value. First NN distribution can be reasonably modeled with a Gaussian law, while 2nd NN distribution fit a nearly symmetric lognormal law. It can observed that both 1st NN distributions are centred on close values while differences can been seen for the 2nd NN. Furthermore, variance is significatly higher for numerically generated microstructures. However, it should be remarked that the experimental distribution relies on a single microstructure while several fibrous geometries should be analysed to retrieve a more representative distribution. Further comparisons should be carried out when supplementary documented data are made available. Nonetheless, mean NN distances of our generated microstructures are rather close to experimental ones which give us confidence on the relevance of representativity of the generation algorithm. By comparing 1st NN distribution for different numbers of perturbations N_p, it can be seen in Fig.5 that distributions become stable from $N_p = 1000$. In a similar fashion, it has been observed that permeability distributions are nearly unchanged from 1000 perturbations, for a same set of input parameters. For the rest of the study, $N_p = 5000$ will be chosen.

2.2. Numerical strategy

Stokes equations are solved on fluid domain Ω_L (Fig.6) using a stabilised FEM approach implemented in Z-Set software [1] which has been widely presented in former articles

[1] http://www.zset-software.com/

[2, 18, 61]. An Algebraic Sub-Grid Scale (ASGS) [19, 38] stabilisation scheme is implemented to circumvent Ladyzhenskaya–Babuška–Brezzi [10] condition with a piecewise linear approximation of both velocity and pressure fields.

Accounting for Navier slip in the weak formulation can be now briefly described, further details are presented in [18]. The weak formulation of the problem is obtained by multiplying Stokes equations by appropriate test functions and then intergrating by parts. This leads to a surface integral term $\mathscr{T}$ on the boundaries of the fluid domain, $\partial\Omega_L$. For single-phase flow, the integral is decomposed into two terms: a Neumann boundary condition term on RVE boundaries (i.e. the imposed stress vector on RVE boundaries), $\mathscr{T}_{\Gamma_N}$, and a complementary term on the fibre contours, $\mathscr{T}_{\Gamma_{LS}}$, that naturally reveals the Navier slip condition:

$$\mathscr{T} = \mathscr{T}_{\Gamma_N} + \mathscr{T}_{\Gamma_{LS}} \tag{7}$$

with:

$$\begin{aligned} \mathscr{T}_{\Gamma_{LS}} &\equiv \int_{\Gamma_{LS}} \boldsymbol{\sigma}\cdot\boldsymbol{n}\cdot\boldsymbol{v}^\star \, d\Gamma \\ &= \int_{\Gamma_{LS}} -\frac{\mu}{\ell_s}\boldsymbol{v}\cdot\boldsymbol{v}^\star \, d\Gamma \end{aligned} \tag{8}$$

by considering Eq.5 and where $\boldsymbol{v}^\star$ is a test function with suitable properties.

Computational times strongly depend on both domain size and V_f. For $V_f = 0.5$ and $L/\bar{r} = 60$, the mesh around 10^6 nodes leading to 3×10^6 degrees of freedom (two per nodes for velocity and one for pressure) (Fig.7). The number of nodes has been optimised using an adaptative mesh: 8 points are regurlarly placed on the contour of each fibre. For each point, the first NN inter-fibre distance is computed to define a mesh size map (Fig.7). This finally permits to retrieve the minimum number of elements (i.e. 8 elements from our tests) within each flow channel between fibres to ensure a good representation of the parabolic Poiseuille-like flow. The full computation chain, from microstructure generation to flow simulations, has been performed on a desktop computer (CPU: i5-8500, 6×3.0 GHz ; RAM: 16 Gb) and lasts approximately 10 minutes with a direct solver for the finite element linear system: around 80% of the computation time is taken by the resolution of the FEM problem. Computational times are thus reasonable enough to generate data massively.

2.3. Boundary conditions and permeability tensor computation

The permeability tensor $\boldsymbol{K}$ (Eq.4) is considered as a continuous random variable: each permeability tensor $\boldsymbol{k}$ computed from a generated microstructure is regarded as a realisation of $\boldsymbol{K}$. The computation of $\boldsymbol{k}$ is detailed in the following.

Considering a given microstructure, constant pressures p_1 and p_2 are applied on opposite boundaries entailing a pressure difference $\Delta p = p_2 - p_1$ (Fig.6). Pressure is weakly imposed through the Cauchy stress tensor: $\boldsymbol{n} \cdot \boldsymbol{\sigma} \cdot \boldsymbol{n} = -p_1$ or $-p_2$ on Γ_N. Note that for this linear approach the computed permeability does not depend on the pressure differential. Since the mesh is periodic, a periodic velocity is easily prescribed on perpendicular edges (Fig.6):

$$\left.\begin{array}{rcl} \boldsymbol{v}(x,0) & = & \boldsymbol{v}(x,L) \\ \boldsymbol{v}(0,y) & = & \boldsymbol{v}(L,y) \end{array}\right\} \text{ for a pressure drop along } \left\{\begin{array}{l} x \text{ direction} \\ y \text{ direction} \end{array}\right. \tag{9}$$

This allows the full permeability tensor $\boldsymbol{k}$ to be computed from outgoing flows (Fig.8). Let's assume that a pressure difference $\Delta_j p$ is imposed over a length L_j, along the j direction characterised by a unit vector $\boldsymbol{e}_j$. The upscaled pressure gradient is usually linearised: $\boldsymbol{\nabla} p_D = (\Delta_j p / L_j)\, \boldsymbol{e}_j$. The upscaled velocity component v_{D_i} is generally defined as $v_{D_i} = Q_i / A_i$ where $Q_i = \displaystyle\int_{A_i} \boldsymbol{v} \cdot \boldsymbol{e}_i \, dA_i$ is the flow-rate through cross-section A_i. Darcy law can thus be rewritten (Eq.4) so that permeability can be computed:

$$k_{ij} = -v_{D_i} \frac{\mu L_j}{\Delta_j p} = -\frac{Q_i}{A_i} \frac{\mu L_j}{\Delta_j p} \tag{10}$$

It is important to notice that the computation of off-diagonal components of permeability tensor from perpendicular outgoing flow is allowed by periodic boundary conditions. A comparable method for permeability calculation can be found in [56]. As a general notation, the overscript bar (e.g. $\bar{k}$) will denote for the rest of the paper the empirical mean computed from realisations.

2.4. Gaussian process regression

Several kinds of variability affect the permeability values in this study. As a consequence, it is relevant to consider the resulting permeability through a regression method that naturally takes into account those variabilities and proposes an uncertainty estimation for interpolation. Moreover, as computation may be expensive, the regression should

be efficient even for small databases. For all these reasons, a Bayesian machine-learning approach, namely Gaussian Process Regression (GPR), is selected here [64]. The basics of GPR are now detailed. GPR is equivalent to kriging [44, 48, 53] even if both approches are different: GPR uses a Bayesian framework while kriging is based on the best linear unbiased predictor.

A dataset D is considered :

$$D = \left\{(X_1, Y_1), ..., (X_N, Y_N)\right\} = \left\{\boldsymbol{X}_D, \boldsymbol{Y}_D\right\} \tag{11}$$

From D, the image Y^* of an new input $X^* \notin D$ through the unknown function to model f is sought. For sake of simplicity, the case $f : \mathbb{R} \to \mathbb{R}$ is presented here even though the approach can be generalised for higher dimension spaces. GPR is based on a probabilistic interpolation of data: f is seen as a random variable. In other terms, the probability of a model *knowing* the dataset D is considered. The latter can be rewritten using Bayes formula. A hypothesis on the prior probability distribution should be then proposed. GPR assumes that the model probability follows a Gaussian process:

$$\forall \boldsymbol{f}_{X_1,...,X_n} = \big(f(X_1), ..., f(X_n)\big), \quad \boldsymbol{f}_{X_1,...,X_n} \sim \mathcal{N}(0, \boldsymbol{C}) \tag{12}$$

where $\boldsymbol{C}$ corresponds to the covariance matrix that can be expressed with a kernel function c according to Mercer's theorem. The choice of the kernel function makes an assumption on the regularity of the function to model. In the context of this study, variations are supposed to be rather smooth leading to consider a common radial basis function:

$$C_{ij} = c(X_i, X_j) = \sigma \exp\left(-\frac{(X_i - X_j)^2}{2\lambda^2}\right) \tag{13}$$

where σ and λ are two hyper-parameters. The previous assumptions on the Gaussian behaviour allows to use related powerful properties. They especially state that Y^* *knowing* D and X^* (i.e. the new wanted output knowing the related new input and the dataset) follows a Gaussian trend with explicit formula for parameters:

$$p(Y^*|D, X^*) \sim \mathcal{N}(\mu^*, \Sigma^*) \tag{14}$$

with:

$$\mu^* = c(X^*, \boldsymbol{X}_D)^T \cdot \big(c(\boldsymbol{X}_D, \boldsymbol{X}_D) + \alpha \boldsymbol{I}\big)^{-1} \cdot \boldsymbol{Y} \tag{15}$$

and

$$\Sigma^* = c(X^*, X^*) - c(X^*, \boldsymbol{X}_D)^T \cdot \left(c(\boldsymbol{X}_D, \boldsymbol{X}_D)^{-1} + \alpha \boldsymbol{I}\right) \cdot c(X^*, \boldsymbol{X}_D) \tag{16}$$

with $c(X^*, \boldsymbol{X}_D) = \left(c(X^*, X_1), ..., c(X^*, X_N)\right)$ and $c(\boldsymbol{X}_D, \boldsymbol{X}_D) = \left(c(X_i, X_j)\right)_{ij}$. Eq.15 should be seen as the most probable output for X^* while Eq.16 is the related uncertainty on interpolation. This is illustrated in Fig.9 as an example where the dataset contains only six (X_i, Y_i) couples: Eq.15 corresponds to the blue continuous line while Eq.16 corresponds to the light blue shaded zone. A noisy GPR formulation is considered here (Eq.15, 16): a diagonal perturbation term $\alpha \boldsymbol{I}$ is added. Such a term has a double interest. First, it adds a flexibility on dataset points. This prevents from overfitting but also allows taking dataset variability into account (Fig.9, 10). Second, the noisy formulation has also a purely numerical role. Indeed, Eq.16 relies on inverting a matrix that can be poorly conditionned due to the use of a quadratic exponential function (Eq.13). Noise terms thus make inversion stable. In the context of this work, we select the noise intensity α to have a physical meaning, it will be equal to the variability observed at each dataset point. At last, it should be remarked that the derivation of hyper-parameters σ and λ have not been detailed yet. Those are classicaly computed afterwards by maximisation of the marginal likelihood function.

3. Results

3.1. RVE determination

The first step of our approach consists in determining the RVE size to ensure the validity of the upscaling process. Classicaly, permeability is computed for increasing domain size. The minimum length to retrieve a reasonable convergence towards an asymptotical value corresponds to the RVE size ℓ_{RVE}. The convergence pattern is characterised by a clear convergence of mean value as well as a decrease of the variability [24]: the domain becomes large enough to capture the statistical information of the medium. The value of ℓ_{RVE} clearly depends on V_f. It can be expected that ℓ_{RVE} diminishes when V_f increases as geometrical arrangement tends towards a hexagonal pattern that can be described with a well-known unit cell [29]. In addition, ℓ_{RVE} can be related to the type of boundary condition that are applied. Indeed, periodic boundary conditions are known to help convergence as it gets rid of edge effects since the space is toroidal [88].

Permeability tensor is thus computed for various domain size ℓ at different V_f values. Domain size is here expressed as a dimensionless quantity :

$$\ell = \frac{L}{\bar{r}} \tag{17}$$

A no-slip condition is first considered at fluid-solid interface as Navier slip is supposed not to have a significant impact on RVE size. For each (ℓ, V_f) couple, 30 microstructures are considered. This allows to determine the RVE related to a given V_f value. We have considered $V_f \in \{0.3, 0.4, 0.5, 0.6\}$ to describe situations from highly porous cases to the ones observed in the manufacture of high performance composite materials. An exemple of convergence plot for permeability of diagonal terms is represented in Fig.11 for both constant and random Gaussian radii. As indicated earlier, microstructures with a constant radius are obtained by setting a coefficient of variability for the fibre radius close to zero (i.e. $C_r \ll 1$).

Those curves follow the expected trend as mean values converge towards a constant value and variability decreases. When convergence is reached for diagonal terms, off-diagonal components are found to be two orders of magnitude lower than diagonal ones. It has thus been chosen to neglect them. Those results follow the conclusions of [56]. It should be reported that, for a given microstructure, discrepancies are observed between off-diagonal terms whereas permeability tensor is generally considered as symmetric. Those differences can be attributed to numerical artefacts or permeability computing method. This is not really problematic as far as the weight of those terms is irrelevant.

The value of ℓ_{RVE} is now estimated. For all V_f values, the coefficient of variability C_k (i.e. the ratio between the standard deviation and the mean value) decreases when ℓ increases until being stable at around 3%. Similar observations can be found in [87] for constant fibre radii. Based on this observation, we first choose to define ℓ_{RVE} as the first value from which C_k becomes lower than 5%. Estimations of ℓ_{RVE} from this criterion are proposed in Table 1. As convergence patterns are similar for both diagonal terms, a single ℓ_{RVE} is indicated for both k_{xx} and k_{yy}. Results follow the expectations as ℓ_{RVE} decreases when V_f value increases. It is also relevant to notice that, for a same V_f value, ℓ_{RVE} is higher for a random radius. Indeed, radius variability brings an additional statistical information: the RVE is then larger in order to grasp it.

However, the convergence criterion may be limited. Indeed, even when dispersion is

stable, distributions and especially mean values can be locally sensitive to the domain size. Broadly speaking, giving a precise value of ℓ_{RVE} is not necessarily straightforward and relevant due to the stochastic character of the study. To circumvent this problem, it has been chosen to consider $\ell_{RVE} \sim 100$ for all V_f. Indeed, this value seems to be large enough to provide convergence in any case. It is also rigourously consistent with the scale separation hypothesis which is the basement of homogeneisation procedures [82]. This choice is critical in terms of computation effort.

3.2. RVEs isotropy

From Fig.11, it can be noticed that k_{xx} and k_{yy} distributions at convergence are very close: this is more clearly illustrated in Fig.12. Both seem to follow a Gaussian trend [8, 90]. A Kolmogorov-Smirnov statistical hypothesis test [37] can be performed to justify rigourously the similarity of the distributions. This test is based on the comparison between the cumulative distribution function of both samples. The associated null hypothesis supposes an equality between both cumulative distribution fonction. A risk of 5% has been chosen. For all V_f values, p-values are retrieved : all are superior to 0.53. As they are significantly higher than the risk, this leads to conserve the null hypothesis:

$$K_{xx} \overset{d}{=} K_{yy} \tag{18}$$

where $\overset{d}{=}$ means "equal in distribution". Considering that the perturbation step of generation algorithm is isotropic, it can be definitively stated that:

$$K_{xx} = K_{yy} \tag{19}$$

This means that microstructures are statistically isotropic in the plane $(\boldsymbol{e}_x, \boldsymbol{e}_y)$ which is consistent with both ergodicity hypothesis and the generation method. Similar observations have been made in [87]. This also explains the irrelevance of off-diagonal terms for RVEs. In the following, permeability will thus be considered as a scalar. In a similar fashion, k will denote realisation of a random permeability variable K.

3.3. Variability related to fibre centre randomness

We first describe the influence of fibre centre location, induced by the proposed generation method, on permeability. For that purpose, permeability for a constant radius

can be compared with various analytical robust models. Those models generally consider unit cells for which fibre centres are placed periodically allowing geometrical simplifications. Gebart permeabilities [29] have thus been considered. A comparison is observed in Fig.13. It can be seen that analytical models do not manage to model the data properly for the V_f values considered. Indeed, geometrical randomness decreases considerably the permeability values. This could have been inferred since the flow channels formed between fibres become more tortuous than for regular packings. The difference between the results from analytical models and those obtained from random microstructures can be measured by studying the mean value, $\bar{\varepsilon}$, of all relative differences ε_i. Mean relative differences between data mean values and Gebart permeabilities (Table 2) are both significantly high. It can be remarked that $\bar{\varepsilon}$ is lower for Gebart's quadratic model. Moreover, it can be seen in Fig.13 that this model is more efficient than the hexagonal one for high V_f value. This is explained by the selected generation algorithm: for high V_f values, the memory of the initial packing still remains. Nevertheless, with little computional efforts, the geometrical stochastic character of the permeability can be highlighted.

The results are now compared to permeability values from similar studies that has been shown to be in agreement with experimental data [8, 87]. The microstructures of these works also show a constant fibre radius while the generation algorithms are different. Results are presented in Fig.14. A good agreement is globally observed as it can be confirmed by computing $\bar{\varepsilon}$. It should be noted that $\bar{\varepsilon}$ is computed from mean values. As a result, it does not take into account the observed permeability distribution. For instance, the mean relative difference for [8] seems to be high while both distributions (Fig.14) seem to be consistent. It should be remarked that results from [8] show a high dispersion ($\sim$ 15%) that may question the representativity of the geometries in consideration. Yet, all the results show a clear linear trend between the logarithm of mean permeability and V_f as it is confirmed by the GPR and its uncertainty (Fig.14). The mean relative difference between data mean values and a linear model is close to 0.5%. As a consequence, for the range of V_f values considered (i.e. $V_f \in [0.3, 0.6]$), it can be assumed:

$$\log\left(\frac{\bar{k}}{\bar{r}^2}\right) \propto V_f \tag{20}$$

As noticed previously, for a given V_f, permeability distribution follows a Gaussian

law with a low coefficient of variability. Values of C_k are presented in Table 3 for various V_f values. The interest of considering a coefficient of variability rather than a standard deviation is to reason with a dimensionless quantity that can be compared for different V_f, which is necessary since permeability spans several orders of magnitude. It can be seen from Table 3 that this variability is globally stable w.r.t. to V_f and close to 3%. This statistical variability can be integrated into the model by multiplying the relation between permeability and fibre volume ratio (Eq.20) by a random variable $\gamma \sim \mathcal{N}(1, 3\%)$:

$$\frac{K}{\bar{r}^2} = \gamma \exp\left(c_1 + c_2 V_f\right) \tag{21}$$

where c_1 and c_2 are the coefficients from linear regression (Eq.20) ($c_1 \approx 1.18$, $c_2 \approx -11.8$). This allows a probabilistic modelling of the permeability behaviour, involving an explicit random variable. This finally leads to a first statistical bounding for permeability of random fibrous media with circular cross-sections.

It should be noticed from Fig.14 that all the results match well for high porosity values. This shows that the generation algorithms are equivalent for low V_f. Indeed, few fibres are observed within the RVEs and consequently, the non-overlapping condition is no more critical. At the opposite, when V_f value is high, the specificities of the selected generation algorithms may affect more directly permeability distributions [87]. However, the overall good agreement between the presented models gives us confidence about the universality of coefficients c_1 and c_2 in similar cases.

3.4. Variability related to radius randomness

The influence of radius randomness on permeability is here investigated. Most of the studies in literature are performed with constant radius which is not consistent with experimental observations. Yet, radius randomness changes flow channel width and tortuosity: it can be expected to alter permeability. As introduced earlier, fibre radii are supposed to follow a normal law with of 10% variability. Permeability values are computed from numerous RVE for constant and random radius. Both histograms are compared in Fig.15. The fibre radius variability does not seem to have a significant impact on permeability distribution. This observation can be confirmed with a Kolmogorov-Smirnov test. For all V_f values considered, each p-value is higher than 20% which leads

to conserve the null hypothesis according to which both samples follow the same distribution. This allows to show that fibre radius variability does not affect significantly permeability. This can be explained as the radii follow a Gaussian law centered in $\bar{r}$. As a result, even if the flow channels width is altered, overall contribution equilibrates which leads to an unsignificant global effect. Such an observation may thus justify the consideration of a constant fibre radius which has several important implications. First, it makes possible to consider a simpler generation algorithm with smaller computation domains (Section 3.1). Then, Eq.21 remains valid for random radii with a variability of 10%. For a higher radius variability (e.g. glass fibres) or for non-circular cross-sections (e.g. flax fibres), those results should be reconsidered.

3.5. Variability related to slip length consideration

We now consider Navier slip (Eq.5) at the fluid-solid interface. As explained in introduction, both analytical and computational upscaling procedures usually assume a no-slip condition while fibre treatment has been experimentally shown to alter fluid flow within the porous medium [25]. For a given microstructure, fluid slip is expected to increase permeability as it gets easier for the liquid to flow across the porous medium. This can be simply highlighted considering a Poiseuille flow between two planes separated by a distance a (Fig.16). Permeability κ can computed analytically by solving Stokes equations, integrating velocity field and then identifying with Darcy law:

$$\kappa = \frac{a^2}{12} + \frac{a\ell_s}{2} \tag{22}$$

When slip length vanishes, Eq.22 corresponds to no-slip permeability. In a free-slip scenario, permeability becomes infinite. Despite the simplicity of this example, it allows to underline the significant importance of slip length on permeability. As a consequence, permeability cannot be only considered as an intrinsic geometrical property like it is quasi-systematically assumed in literature. On the contrary, permeability should be related to fluid shear that has two origins: the tortuosity of flow channels (i.e. a geometrical contribution) and the condition at liquid/solid interface. This especially explains why permeability cannot be defined in a Poiseuille flow with free-slip (Eq.22) as the fluid is not sheared. However, when the fluid is newtonian with a no-slip condition, the interface

contribution does no longer induce variability and permeability can be considered as a morphological property of the medium.

The influence of slip length on permeability is represented in Fig.17 for a given random microstructure with random radii. Permeability computed with fluid slip K_s is bounded between no-slip K and free-slip permeabilities K_{fs} as Navier slip (Eq.5) generalises both conditions. We have considered slip length values significantly superior to the ones encountered experimentally [42, 43] (typically $10^{-9} - 10^{-6}$ m) in order to capture and characterise precisely the transition between regimes. GPR has been performed to model the trend: the related uncertainty is relatively low. Mean value of GPR perfectly match a sigmoid model. The following relation can thus be proposed:

$$K_s = K + \frac{K_{fs} - K}{1 + \frac{1}{2}\frac{\bar{r}}{\ell_s}} = K\left[1 - \frac{1-\alpha}{1 + \frac{1}{2}\frac{\bar{r}}{\ell_s}}\right] \tag{23}$$

where $\alpha = K_{fs}/K$ represents the amplitude of fluid slip phenomenon.

The influence of slip length on permeability can be now expressed for numerous microstructures at a given V_f value (Fig.18). This allows to integrate the statistical variability into the study of fluid slip. It is relevant to notice in Fig.18 that microstructure statistical variability, even with random radii, is relatively low in comparison with the curve amplitude due to the slip effect. The coefficient of variability is globally similar for all the ℓ_s values. Once again, GPR is performed from mean values with a noise equal to the variance. It also follows a sigmoid trend which confirms the validity of Eq.23. In addition, Eq.23 seems to hold well for different V_f values without further fit parameters, as it can be observed in Table 4. This equation can also be useful in practice to determine slip length values as discussed in Section 4.2.

We expect the fluid slip importance to rise when fibre volume fraction gets higher as the slip surface increases. We thus consider α as a function of V_f (Fig.19). It should be noticed that the ratio between no-slip and free-slip permeabilities can reach a decade for V_f of interest in high performance composites. As the relation between the logarithm of α and V_f is linear in a first approach, we write:

$$\log(\alpha) = \beta V_f \tag{24}$$

where β is the slope of the linear regression ($\beta \approx 3.65$) This relation can be injected to

Eq.23 to get:

$$K_s = K\left[1 - \frac{1-\exp(\beta V_f)}{1+\frac{1}{2}\frac{\bar{r}}{\ell_s}}\right] \tag{25}$$

Eq.25 requires no-slip permeability K which can be retrieved numerically or experimentally in practice. In the context of this work, K carries the stochastic information of the model: it is expressed as a random variable. Its expression is directly linked to V_f as proposed previously in Eq.21. This finally provides a general bounding of permeability including both fluid slip and statistical variability:

$$K_s = \bar{r}^2\gamma\exp\left(c_1 + c_2 V_f\right)\left[1 - \frac{1-\exp(\beta V_f)}{1+\frac{1}{2}\frac{\bar{r}}{\ell_s}}\right] \tag{26}$$

It can be remarked from the mathematical expression of the sigmoid model (Eq.23) that the transition zone from no-slip to free-slip regime is not affected by V_f. This means that, indepedently from V_f, the regime transition always occurs for slip lengths between 10^{-9}m and 10^{-4}m. Those values are close to realistic values of ℓ_s meaning that fluid slip may affect permeability in practice (Section 4.2). Finally, permeability can be expressed as a function of the slip length and V_f that are two independent variables. Both analytical (Eq.26) and GPR approaches are in very good agreement and allow a good modelling of data. The mean relative difference between analytical model and data is about 2.35%. It should be remarked that Eq.26 only holds for the transverse permeability in a 2D case. Longitudinal permeability should also be considered [22, 69] to retrieve a more complete and realistic model. Further studies should be performed to clarify this point, that is out of the scope of this work.

4. Discussion

4.1. On permeability variability

Variability of permeability values is now discussed. We have highlighted that common analytical models based on geometrical simplifications cannot inherently model random fibrous medium permeability. As noticed before, for a given V_f value, this variability is approximately 3% regardless of radius randomness. It seems acceptable to consider this variability as low. This observation gives an interesting insight to studies that aim at

finding the best correlations between permeability and various microstructural parameters [54, 87]. Indeed, while V_f is the most straightforward parameter to describe a fibrous microstructures, it captures nearly 95% of the observed variability. This confirms that V_f is a first-order parameter for the characterisation of fibrous media permeability as it is generally assumed. Therefore further morphological parameters may allow to describe the remaining variability or else to propose a better correlation with permeability than V_f. Those observations regarding the low variability of permeability values computed from RVEs may also justify the use of deterministic relations. Depending on the context of further works, this may be justified as far as RVEs are supposed to grasp the statistical variability of a medium.

4.2. Numerical application for fluid slip influence

In the previous sections, theoretical influence of slip length on permeability has been examined. However, as a wide range of ℓ_s were considered, some values were considerably higher than the orders of magnitude that are typically found in literature. As a consequence, it seems relevant to study the influence of slip length for more realistic values.

As a numerical application, we consider here $\bar{r} = 3.5\mu m$, $V_f = 0.6$, that is a typical value for high-performance applications and $\ell_s = 8 \pm 2$ nm that was experimentally estimated in [51] for water on a plane graphite surface, assuming that this slip length can characterise carbon fibre/fluid interactions. The extreme values have been considered for slip length (i.e. 6 nm and 10 nm). It should be remarked that those values do not take surface roughness effects into account [51]: such additional effects would tend to increase slip length. By application of Eq.25, results presented in Table 5 are retrieved: assuming Gaussian distributions, intervals that contain 95% of the distributions can be proposed. This leads to a confidence interval $[3.24\ ,\ 3.71]\times10^{-14}m^2$ for permeability. Considering mean values, it can be seen that the relative difference w.r.t. no-slip situation is near 3%. This is comparable with statistical variability (Section 4.1). In other words, taking fluid slip into account or not would lead, at least, to an uncertainty as large as statistical variability. This can justify the importance of fluid slip in real-world applications, for example in composite materials manufacturing. This also confirms experimental observations from [25] where sizing (i.e. a chemical surface treatment of fibres) can divide

permeability values up to 4 times. Moreover it should be noticed that slip length of $10^{-6} - 10^{-4}$ m can be found in [66]. Even if those values were back-calculated for transient multiphase flow involving capillarity, they would lead to huge differences between permeability computed with fluid slip or no-fluid slip conditions (Table 5). This highlights the necessity of accurate slip length value for the resin/carbon couple under consideration in LCM processes. It should be also noticed that the difference between free-slip and no-slip permeabilities is close to one order of magnitude (Table 5, Fig.19). As a consequence, the bounding of permeability related to fluid slip is particularly wide in comparison with statistical bounds.

Finally, Eq.23 can also be useful for experimental determination of slip length from real-world fibrous materials. Indeed, the equation does not show any tuning parameter for a given microstructure. Thereby, permeability K should be first measured experimentally. Then, digitisation of the medium (e.g. through X-ray tomography) may allow to estimate K_{fs} with numerical simulation. This may lead to retrieve the slip length from Eq.23. Naturally, this would rely on the validity of Eq.23: further studies should be carried out to show the relevance of the expression especially for other radius distributions or for random slip length values within a microstructure.

5. Conclusion

The main results of the study are summarised here:

- Numerous periodic fibrous microstructures have been generated numerically through a simple and fast algorithm. The RVE size has been determined through a convergence study of permeability components. To simplify the determination of RVE size, it has been set to meet the scale separation hypothesis.

- A statistical study has been performed using several data-related tools such as Kolmogorov-Smirnov statistical hypothesis testing or Gaussian process regression: those allowed to take variability into account in a response model. The permeability tensor can thus be reduced to a single scalar value as long as isotropy is met statistically.

- Two kinds of geometrical variability have been considered. Fibre center location randomness has been shown to alter significantly permeability values, highlighting the importance of a statistical modelling. Considering a Gaussian distribution for fibre radius — with a radius variability up to 10% — has been shown to have a negligible impact on permeability.

- Permeability has been then found to follow a Gaussian distribution with a relatively low coefficient of variability ($\sim 3\%$) providing a narrow confidence interval for permeability. This has also lead to consider V_f as a relevant morphological parameter for permeability characterisation as it explains on its own more than 95% of the variability.

- Fluid slip at fibre/liquid interface has been taken into account. A sigmoid transition has been observed between no-slip and free-slip regimes. This model has been then connected to the early statistical study to get a global equation that encompasses both phenomena. This has finally provided a double bounding for permeability.

Acknowledgement

The authors would like to thank M. Blais and R. Le Riche for helpful discussion.

References

[1] Abdallah, B., Willot, F., Jeulin, D., 2015. Stokes flow through a boolean model of spheres: Representative volume element. Transport in porous media 109 (3), 711–726.

[2] Abou Orm, L., Blais, M., Moulin, N., Bruchon, J., Drapier, S., 2014. A robust monolithic approach for resin infusion based process modelling. In: Key Engineering Materials. Vol. 611. Trans Tech Publ, pp. 306–315.

[3] Ali, M., Umer, R., Khan, K., Bickerton, S., Cantwell, W., 2018. Non-destructive evaluation of through-thickness permeability in 3d woven fabrics for composite fan blade applications. Aerospace Science and Technology 82, 520–533.

[4] Andrienko, D., Dünweg, B., Vinogradova, O. I., 2003. Boundary slip as a result of a prewetting transition. The Journal of chemical physics 119 (24), 13106–13112.

[5] Arbter, R., Beraud, J., Binetruy, C., Bizet, L., Bréard, J., Comas-Cardona, S., Demaria, C., Endruweit, A., Ermanni, P., Gommer, F., et al., 2011. Experimental determination of the permeability of textiles: a benchmark exercise. Composites Part A: Applied Science and Manufacturing 42 (9), 1157–1168.

[6] Auriault, J., 1991. Heterogeneous medium. Is an equivalent macroscopic description possible? International journal of engineering science 29 (7), 785–795.

[7] Bazant, M. Z., Vinogradova, O. I., 2008. Tensorial hydrodynamic slip. Journal of Fluid Mechanics 613, 125–134.

[8] Bodaghi, M., Catalanotti, G., Correia, N., 2016. On the statistics of transverse permeability of randomly distributed fibers. Composite Structures 158, 323–332.

[9] Bodaghi, M., Lomov, S., Simacek, P., Correia, N., Advani, S., 2019. On the variability of permeability induced by reinforcement distortions and dual scale flow in liquid composite moulding: A review. Composites Part A: Applied Science and Manufacturing 120, 188–210.

[10] Brezzi, F., Fortin, M., 2012. Mixed and hybrid finite element methods. Vol. 15. Springer Science & Business Media.

[11] Bruschke, M. V., Advani, S., 1993. Flow of generalized newtonian fluids across a periodic array of cylinders. Journal of Rheology 37 (3), 479–498.

[12] Buryachenko, V., Pagano, N., Kim, R., Spowart, J., 2003. Quantitative description and numerical simulation of random microstructures of composites and their effective elastic moduli. International journal of solids and structures 40 (1), 47–72.

[13] Calado, V. M., Advani, S. G., 1996. Effective average permeability of multi-layer preforms in resin transfer molding. Composites Science and Technology 56 (5), 519–531.

[14] Carman, P. C., 1937. Fluid flow through granular beds. Trans. Inst. Chem. Eng. 15, 150–166.

[15] Catalanotti, G., 2016. On the generation of rve-based models of composites reinforced with long fibres or spherical particles. Composite Structures 138, 84–95.

[16] Chen, J., Kim, Y. J., Hwang, W. R., 2020. General criteria for the estimation of effective slip length over corrugated surfaces. Microfluidics and Nanofluidics 24 (9), 1–15.

[17] Chen, X., Papathanasiou, T. D., 2008. The transverse permeability of disordered fiber arrays: a statistical correlation in terms of the mean nearest interfiber spacing. Transport in Porous Media 71 (2), 233–251.

[18] Chevalier, L., Bruchon, J., Moulin, N., Liotier, P.-J., Drapier, S., 2018. Accounting for local capillary effects in two-phase flows with relaxed surface tension formulation in enriched finite elements. Comptes Rendus Mécanique 346 (8), 617–633.

[19] Codina, R., 2001. A stabilized finite element method for generalized stationary incompressible flows. Computer Methods in Applied Mechanics and Engineering 190 (20-21), 2681–2706.

[20] Comas-Cardona, S., Groenenboom, P., Binetruy, C., Krawczak, P., 2005. A generic mixed fe-sph method to address hydro-mechanical coupling in liquid composite moulding processes. Composites Part A: Applied Science and Manufacturing 36 (7), 1004–1010.

[21] Darcy, H., 1856. Les fontaines publiques de la ville de Dijon: exposition et application... Victor

Dalmont.

[22] DeValve, C., Pitchumani, R., 2012. An analytical model for the longitudinal permeability of aligned fibrous media. Composites science and technology 72 (13), 1500–1507.

[23] Digonnet, H., Coupez, T., Laure, P., Silva, L., 2019. Massively parallel anisotropic mesh adaptation. The International Journal of High Performance Computing Applications 33 (1), 3–24.

[24] Du, X., Ostoja-Starzewski, M., 2006. On the size of representative volume element for Darcy law in random media. Proceedings of the Royal Society A: Mathematical, Physical and Engineering Sciences 462 (2074), 2949–2963.

[25] Dukkipati, R. K., 2007. Experimental investigation of fiber sizing-test fluid interaction for in-plane permeability measurements of continuous fibers. Ph.D. thesis, Wichita State University.

[26] Durville, D., 2010. Simulation of the mechanical behaviour of woven fabrics at the scale of fibers. International journal of material forming 3 (2), 1241–1251.

[27] Feuillebois, F., Bazant, M. Z., Vinogradova, O. I., 2009. Effective slip over superhydrophobic surfaces in thin channels. Physical review letters 102 (2), 026001.

[28] Feuillebois, F., Bazant, M. Z., Vinogradova, O. I., 2010. Transverse flow in thin superhydrophobic channels. Physical Review E 82 (5), 055301.

[29] Gebart, B. R., 1992. Permeability of unidirectional reinforcements for rtm. Journal of composite materials 26 (8), 1100–1133.

[30] Geoffre, A., Wielhorski, Y., Moulin, N., Bruchon, J., Drapier, S., Liotier, P.-J., 2020. Influence of intra-yarn flows on whole 3d woven fabric numerical permeability: from Stokes to Stokes-Darcy simulations. International Journal of Multiphase Flow 129, 103349.

[31] Ghosh, S., Nowak, Z., Lee, K., 1997. Quantitative characterization and modeling of composite microstructures by voronoi cells. Acta Materialia 45 (6), 2215–2234.

[32] Gitman, I., Askes, H., Sluys, L., 2007. Representative volume: Existence and size determination. Engineering fracture mechanics 74 (16), 2518–2534.

[33] Grufman, C., Ellyin, F., 2007. Determining a representative volume element capturing the morphology of fibre reinforced polymer composites. Composites science and technology 67 (3-4), 766–775.

[34] Gusev, A. A., Hine, P. J., Ward, I. M., 2000. Fiber packing and elastic properties of a transversely random unidirectional glass/epoxy composite. Composites Science and Technology 60 (4), 535–541.

[35] He, X., Luo, L.-S., 1997. Lattice boltzmann model for the incompressible Navier–Stokes equation. Journal of statistical Physics 88 (3-4), 927–944.

[36] Hill, R., 1963. Elastic properties of reinforced solids: some theoretical principles. Journal of the Mechanics and Physics of Solids 11 (5), 357–372.

[37] Hodges, J. L., 1958. The significance probability of the smirnov two-sample test. Arkiv för Matematik 3 (5), 469–486.

[38] Hughes, T. J., 1995. Multiscale phenomena: Green's functions, the dirichlet-to-neumann formulation, subgrid scale models, bubbles and the origins of stabilized methods. Computer methods in applied mechanics and engineering 127 (1-4), 387–401.

[39] Huh, C., Scriven, L. E., 1971. Hydrodynamic model of steady movement of a solid/liquid/fluid

contact line. Journal of colloid and interface science 35 (1), 85–101.

[40] Ismail, Y., Yang, D., Ye, J., 2016. Discrete element method for generating random fibre distributions in micromechanical models of fibre reinforced composite laminates. Composites Part B: Engineering 90, 485–492.

[41] Jiménez Bolaños, S., Vernescu, B., 2017. Derivation of the Navier slip and slip length for viscous flows over a rough boundary. Physics of Fluids 29 (5), 057103.

[42] Joseph, P., Tabeling, P., 2005. Direct measurement of the apparent slip length. Physical Review E 71 (3), 035303.

[43] Kobryn, A., Kovalenko, A., 2011. Slip boundary conditions in nanofluidics from the molecular theory of solvation. Molecular Simulation 37 (8), 733–737.

[44] Krige, D. G., 1951. A statistical approach to some basic mine valuation problems on the witwatersrand. Journal of the Southern African Institute of Mining and Metallurgy 52 (6), 119–139.

[45] Kumar, A., Datta, S., Kalyanasundaram, D., 2016. Permeability and effective slip in confined flows transverse to wall slippage patterns. Physics of Fluids 28 (8), 082002.

[46] Kurotani, Y., Tanaka, H., 2020. A novel physical mechanism of liquid flow slippage on a solid surface. Science advances 6 (13), eaaz0504.

[47] Lauga, E., Brenner, M., Stone, H., 2007. Microfluidics: The No-Slip Boundary Condition. Springer Berlin Heidelberg, Berlin, Heidelberg, pp. 1219–1240.

[48] Le Gratiet, L., 2013. Multi-fidelity gaussian process regression for computer experiments. Ph.D. thesis.

[49] Liu, J., Chen, L., Xie, J., Lin, Z., 2020. Micro-flow model with a new algorithm of random fiber distribution over the transverse cross-section. Polymer Composites.

[50] Lomov, S. V., Huysmans, G., Luo, Y., Parnas, R., Prodromou, A., Verpoest, I., Phelan, F., 2001. Textile composites: modelling strategies. Composites Part A: applied science and manufacturing 32 (10), 1379–1394.

[51] Maali, A., Cohen-Bouhacina, T., Kellay, H., 2008. Measurement of the slip length of water flow on graphite surface. Applied Physics Letters 92 (5), 053101.

[52] Maciel, A., Salas, V., Soltero, J., Guzmán, J., Manero, O., 2002. On the wall slip of polymer blends. Journal of Polymer Science Part B: Polymer Physics 40 (4), 303–316.

[53] Matheron, G., 1963. Principles of geostatistics. Economic geology 58 (8), 1246–1266.

[54] Matsumura, Y., Jackson, T., 2014. Numerical simulation of fluid flow through random packs of cylinders using immersed boundary method. Physics of Fluids 26 (4), 043602.

[55] Melro, A., Camanho, P., Pinho, S., 2008. Generation of random distribution of fibres in long-fibre reinforced composites. Composites Science and Technology 68 (9), 2092–2102.

[56] Nabovati, A., Llewellin, E. W., Sousa, A. C., 2009. A general model for the permeability of fibrous porous media based on fluid flow simulations using the lattice boltzmann method. Composites Part A: Applied Science and Manufacturing 40 (6-7), 860–869.

[57] Navier, C., 1823. Mémoire sur les lois du mouvement des fluides. Mémoires de l'Académie Royale des Sciences de l'Institut de France 6 (1823), 389–440.

[58] Nedanov, P. B., Advani, S. G., 2002. A method to determine 3d permeability of fibrous reinforcements. Journal of composite materials 36 (2), 241–254.

[59] Neto, C., Evans, D. R., Bonaccurso, E., Butt, H.-J., Craig, V. S., 2005. Boundary slip in newtonian liquids: a review of experimental studies. Reports on progress in physics 68 (12), 2859.

[60] Ngo, N., Tamma, K. K., 2001. Microscale permeability predictions of porous fibrous media. International Journal of Heat and Mass Transfer 44 (16), 3135–3145.

[61] Pacquaut, G., Bruchon, J., Moulin, N., Drapier, S., 2012. Combining a level-set method and a mixed stabilized p1/p1 formulation for coupling Stokes–Darcy flows. International Journal for Numerical Methods in Fluids 69 (2), 459–480.

[62] Park, C. H., Lebel, A., Saouab, A., Bréard, J., Lee, W. I., 2011. Modeling and simulation of voids and saturation in liquid composite molding processes. Composites Part A: Applied science and manufacturing 42 (6), 658–668.

[63] Ramos-Alvarado, B., Kumar, S., Peterson, G., 2016. Hydrodynamic slip length as a surface property. Physical Review E 93 (2), 023101.

[64] Rasmussen, C. E., 2003. Gaussian processes in machine learning. In: Summer School on Machine Learning. Springer, pp. 63–71.

[65] Ripley, B. D., 1977. Modelling spatial patterns. Journal of the Royal Statistical Society: Series B (Methodological) 39 (2), 172–192.

[66] Rougier, V., Cellier, J., Gomina, M., Bréard, J., 2020. Slip transition in dynamic wetting for a generalized Navier boundary condition. Journal of Colloid and Interface Science 583, 448–458.

[67] Senthil Kumar, V., Kumaran, V., 2005. Voronoi cell volume distribution and configurational entropy of hard-spheres. The Journal of chemical physics 123 (11), 114501.

[68] Sharma, H., Gaddam, A., Agrawal, A., Joshi, S. S., 2019. Slip flow through microchannels with lubricant-infused bi-dimensional textured surfaces. Microfluidics and Nanofluidics 23 (2), 28.

[69] Shou, D., Ye, L., Fan, J., 2015. On the longitudinal permeability of aligned fiber arrays. Journal of Composite Materials 49 (14), 1753–1763.

[70] Standnes, D. C., 2018. Implications of molecular thermal fluctuations on fluid flow in porous media and its relevance to absolute permeability. Energy & Fuels 32 (8), 8024–8039.

[71] Stone, H. A., Stroock, A. D., Ajdari, A., 2004. Engineering flows in small devices: microfluidics toward a lab-on-a-chip. Annu. Rev. Fluid Mech. 36, 381–411.

[72] Swaminathan, S., Ghosh, S., Pagano, N., 2006. Statistically equivalent representative volume elements for unidirectional composite microstructures: Part i-without damage. Journal of Composite Materials 40 (7), 583–604.

[73] Taylor, C., Hood, P., 1973. A numerical solution of the Navier-Stokes equations using the finite element technique. Computers & Fluids 1 (1), 73–100.

[74] Trias, D., Costa, J., Mayugo, J., Hurtado, J., 2006. Random models versus periodic models for fibre reinforced composites. Computational materials science 38 (2), 316–324.

[75] Trias, D., Costa, J., Turon, A., Hurtado, J., 2006. Determination of the critical size of a statistical representative volume element (SRVE) for carbon reinforced polymers. Acta materialia 54 (13),

3471–3484.

[76] Trochu, F., Ruiz, E., Achim, V., Soukane, S., 2006. Advanced numerical simulation of liquid composite molding for process analysis and optimization. Composites Part A: applied science and manufacturing 37 (6), 890–902.

[77] Vaughan, T., McCarthy, C., 2010. A combined experimental–numerical approach for generating statistically equivalent fibre distributions for high strength laminated composite materials. Composites Science and Technology 70 (2), 291–297.

[78] Venkatesan, J., Ganesan, S., 2015. On the Navier-slip boundary condition for computations of impinging droplets. In: 2015 IEEE 22nd International Conference on High Performance Computing Workshops. IEEE, pp. 2–11.

[79] Vernet, N., Ruiz, E., Advani, S., Alms, J., Aubert, M., Barburski, M., Barari, B., Beraud, J., Berg, D., Correia, N., et al., 2014. Experimental determination of the permeability of engineering textiles: Benchmark ii. Composites Part A: Applied Science and Manufacturing 61, 172–184.

[80] Vinogradova, O. I., 1995. Drainage of a thin liquid film confined between hydrophobic surfaces. Langmuir 11 (6), 2213–2220.

[81] Vinogradova, O. I., Belyaev, A. V., 2011. Wetting, roughness and flow boundary conditions. Journal of Physics: Condensed Matter 23 (18), 184104.

[82] Whitaker, S., 1986. Flow in porous media i: A theoretical derivation of Darcy's law. Transport in porous media 1 (1), 3–25.

[83] Wiegmann, A., 2007. Computation of the permeability of porous materials from their microstructure by fff-stokes, fraunhofer itwm kaiserslautern. Tech. rep., Technical Report 129.

[84] Wongsto, A., Li, S., 2005. Micromechanical fe analysis of ud fibre-reinforced composites with fibres distributed at random over the transverse cross-section. Composites Part A: Applied Science and Manufacturing 36 (9), 1246–1266.

[85] Yang, L., Yan, Y., Ran, Z., Liu, Y., 2013. A new method for generating random fibre distributions for fibre reinforced composites. Composites Science and Technology 76, 14–20.

[86] Yazdchi, K., Luding, S., 2013. Upscaling and microstructural analysis of the flow-structure relation perpendicular to random, parallel fiber arrays. Chemical engineering science 98, 173–185.

[87] Yazdchi, K., Srivastava, S., Luding, S., 2012. Micro–macro relations for flow through random arrays of cylinders. Composites Part A: Applied Science and Manufacturing 43 (11), 2007–2020.

[88] Yvonnet, J., 2019. Computational Homogenization of Heterogeneous Materials with Finite Elements. Solid Mechanics and Its Applications. Springer International Publishing.

[89] Zeng, X., Brown, L. P., Endruweit, A., Matveev, M., Long, A. C., 2014. Geometrical modelling of 3d woven reinforcements for polymer composites: Prediction of fabric permeability and composite mechanical properties. Composites Part A: Applied Science and Manufacturing 56, 150–160.

[90] Zhang, F., Comas-Cardona, S., Binetruy, C., 2012. Statistical modeling of in-plane permeability of non-woven random fibrous reinforcement. Composites science and technology 72 (12), 1368–1379.

[91] Zhu, Y., Granick, S., 2002. Limits of the hydrodynamic no-slip boundary condition. Physical review letters 88 (10), 106102.

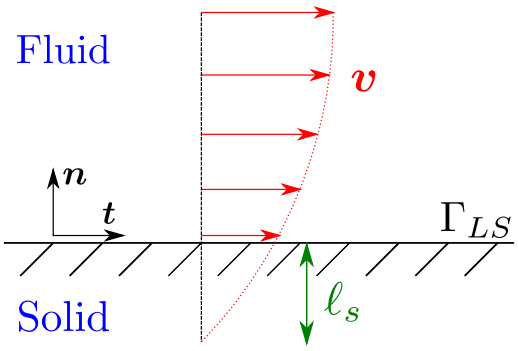

Figure 1: Fluid slip and slip length

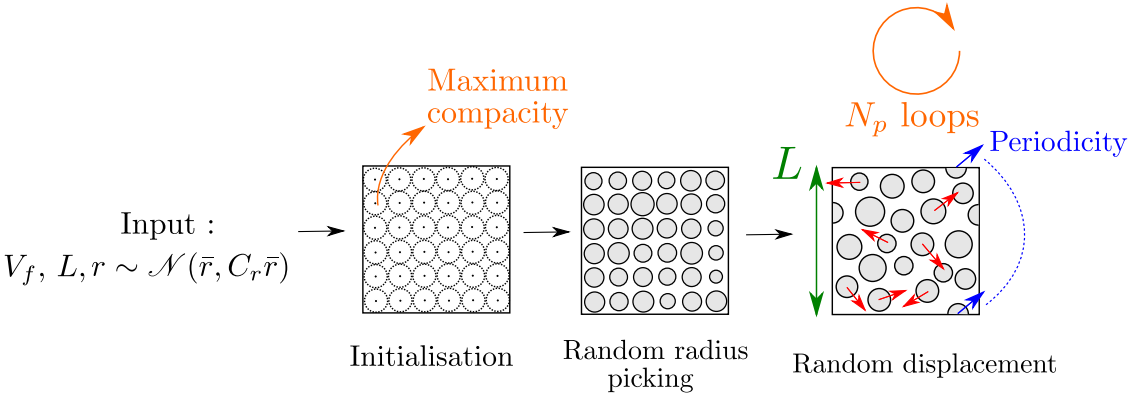

Figure 2: Algorithm for microstructure generation

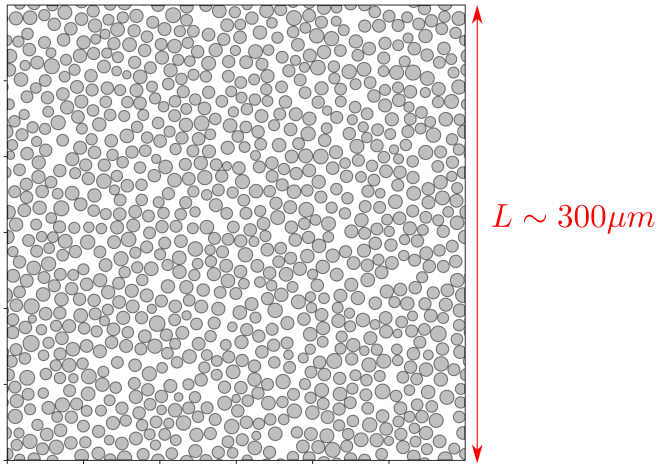

Figure 3: A numerically generated microstructure ($V_f = 0.5$, $r \sim \mathcal{N}(\bar{r}, 0.1\bar{r})$, $L/\bar{r} \sim 85$)

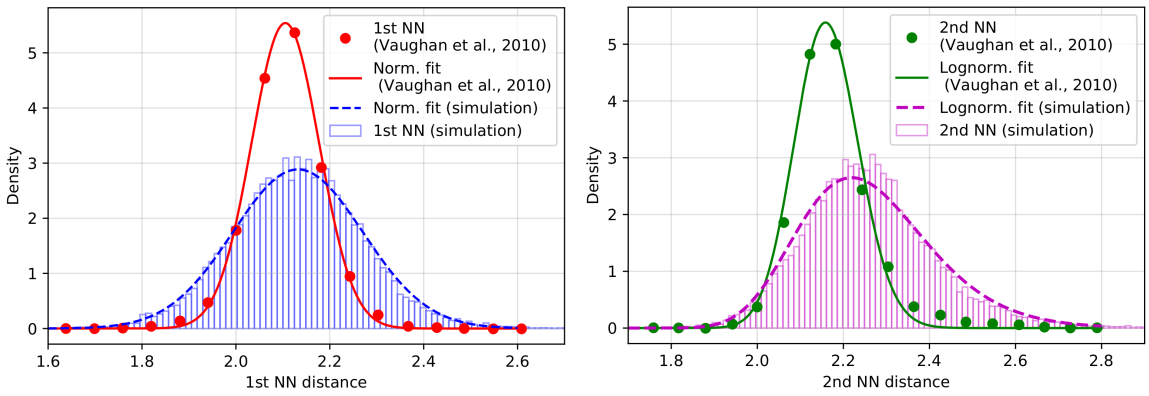

Figure 4: Nearest neighbour distance distributions normalised by $\bar{r}$ ($\sim 2.3 \times 10^4$ generated microstructures,$V_f = 0.59$, $N_p > 1000$)

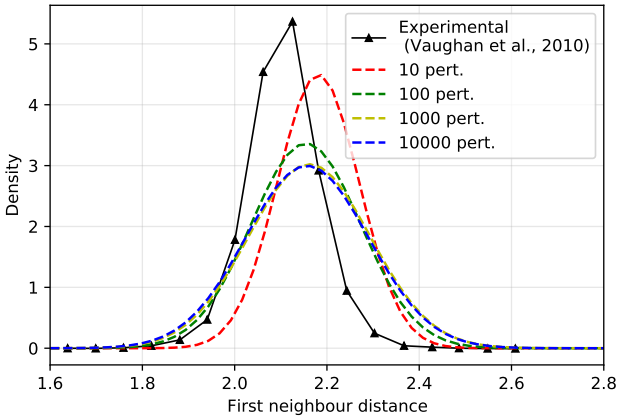

Figure 5: Gaussian fit of first nearest neighbour distance distribution for various N_p values ($V_f = 0.59$)

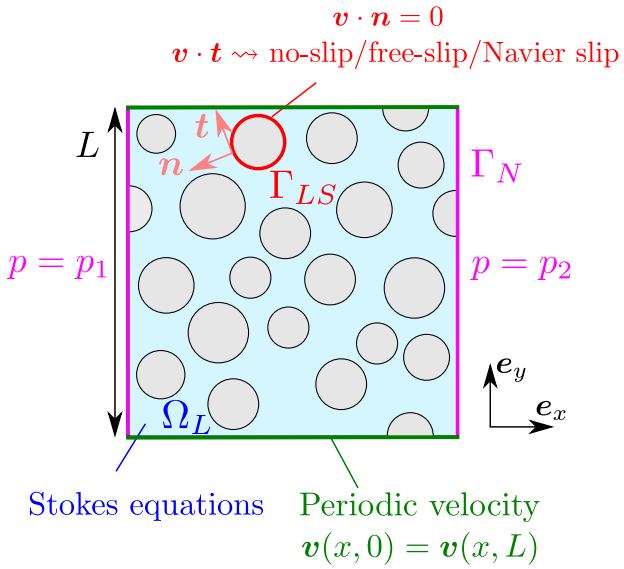

Figure 6: Domains, equations and boundary conditions for a flow in the x direction

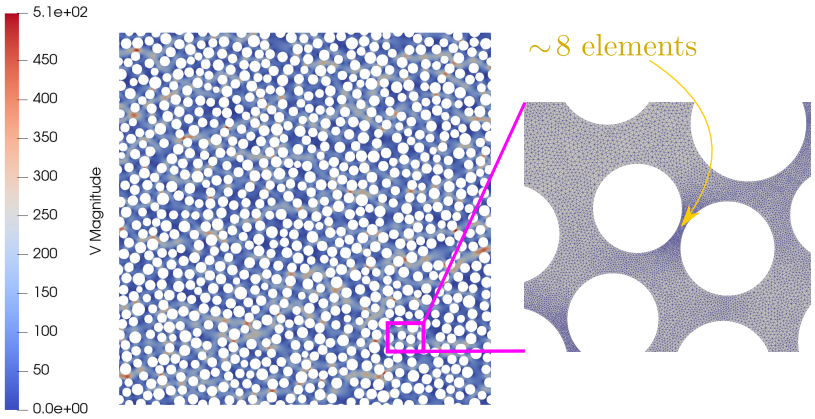

Figure 7: Numerical flow simulation (velocity magnitude field, $\times 10^{-3}$ mm/s) and adapted mesh

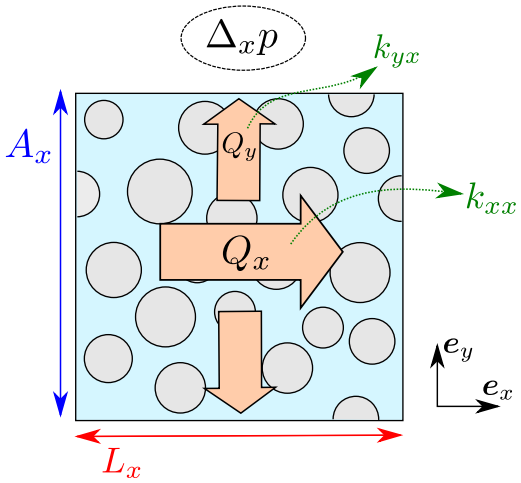

Figure 8: Illustration of the permeability computation method for a pressure gradient along x direction

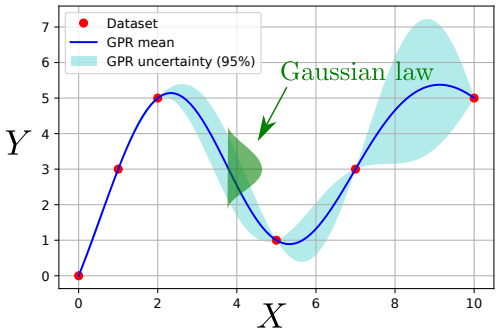

Figure 9: Illustration of noiseless GPR

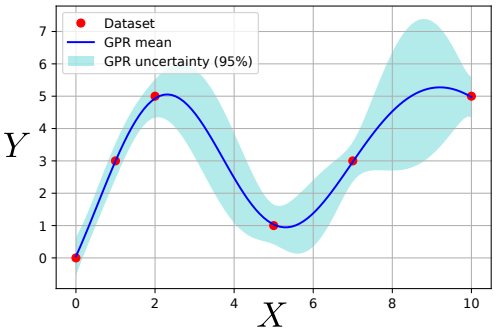

Figure 10: Illustration of noisy GPR

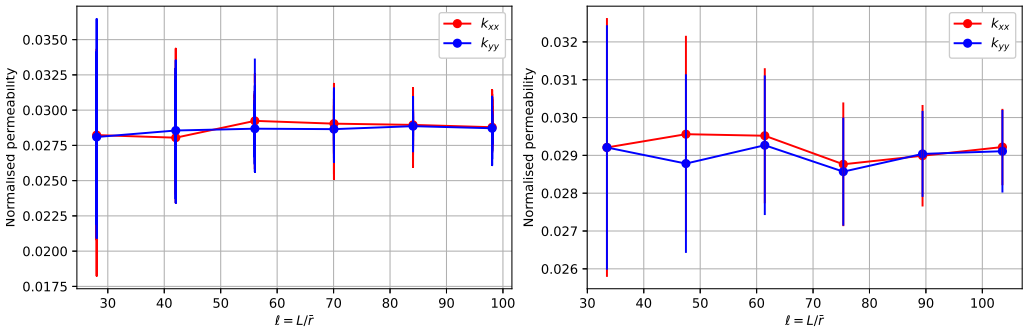

Figure 11: Convergence plot for diagonal terms: mean values and standard deviations ($V_f = 0.4$, left: constant radius, right: random radius)

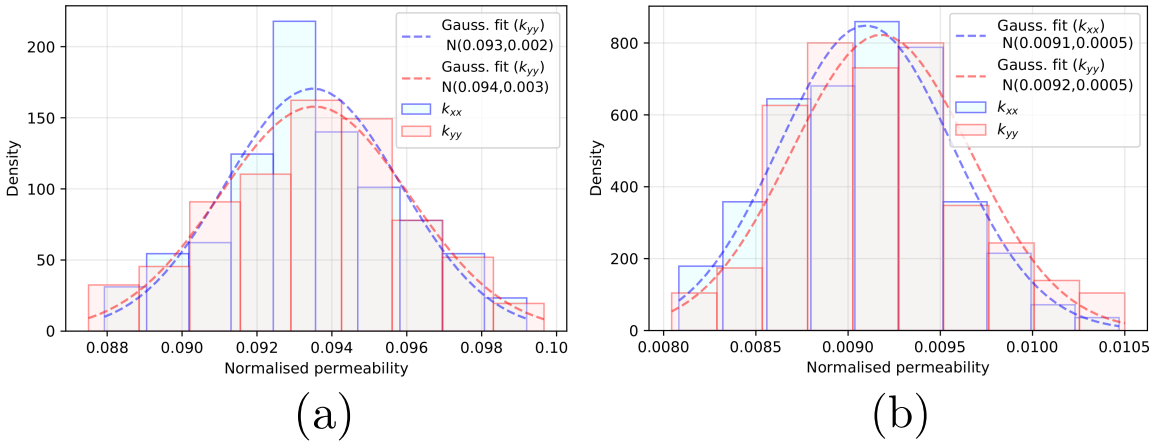

Figure 12: Histograms of diagonal permeabilities normalised by $\bar{r}^2$ ((a) $V_f = 0.3$, (b) $V_f = 0.5$)

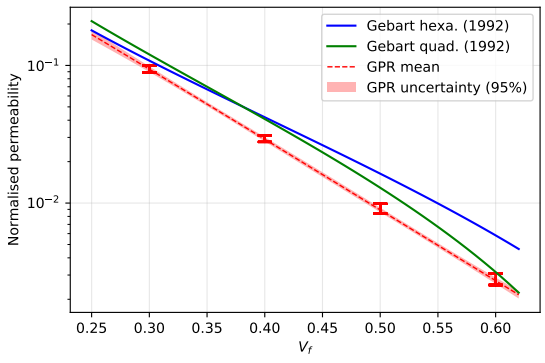

Figure 13: Permeability normalised by $\bar{r}^2$ as a function of V_f: influence of fibres center randomness

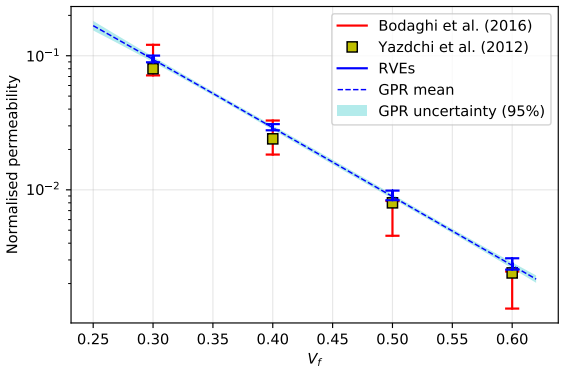

Figure 14: Permeability normalised by $\bar{r}^2$ as a function of V_f: comparison with other studies

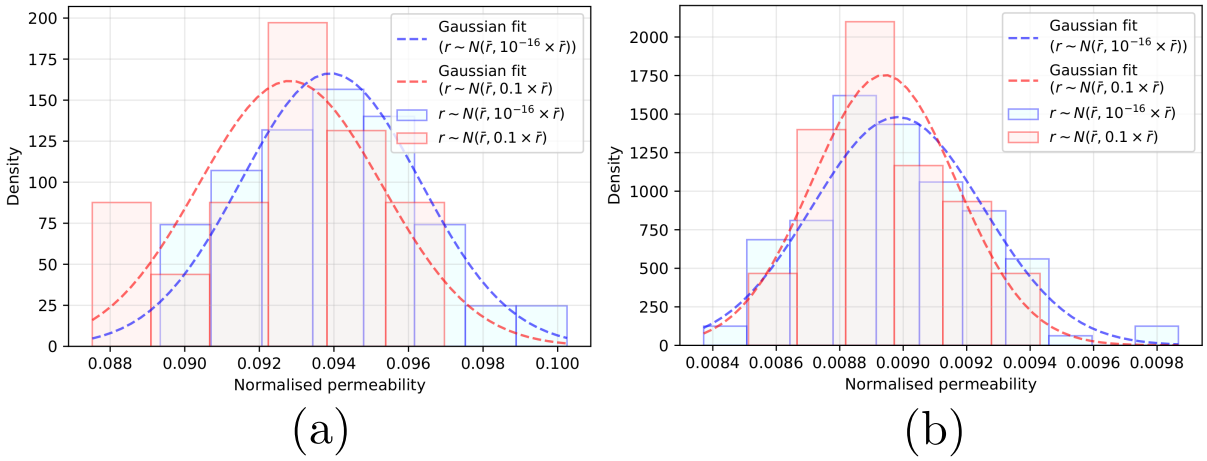

Figure 15: Histogram of permeability normalised by $\bar{r}^2$ for constant and random radii ((a): $V_f = 0.3$, (b): $V_f = 0.5$)

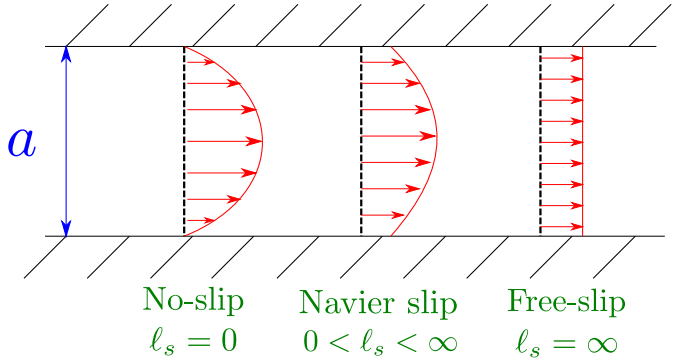

Figure 16: Poiseuille flow and slip length

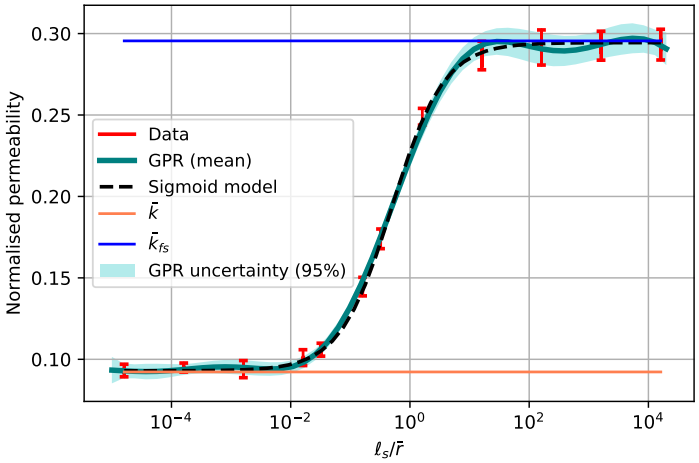

Figure 18: Permeability normalised by $\bar{r}^2$ as a function of slip length with consideration of statistical variability ($V_f = 0.3$, 30 RVEs for each ℓ_s value)

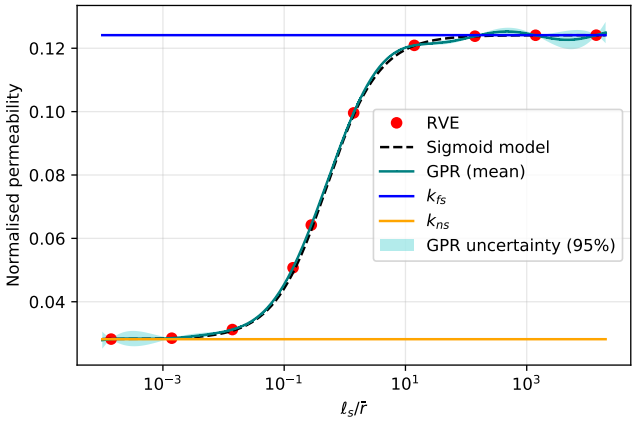

Figure 17: Permeability normalised by $\bar{r}^2$ as a function of slip length for a given microstructure ($V_f = 0.4$)

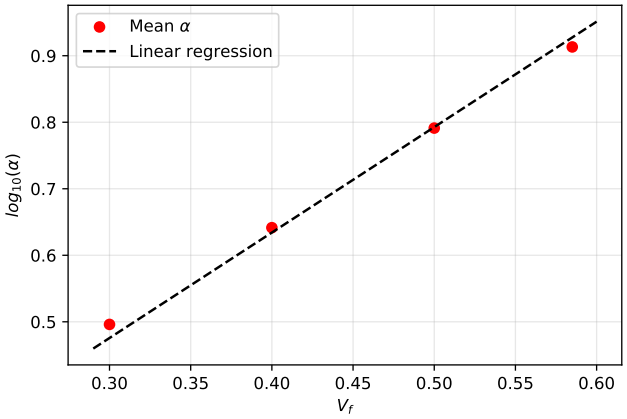

Figure 19: Decimal logarithm of mean α as a function of V_f

	$V_f = 0.3$	$V_f = 0.4$	$V_f = 0.5$	$V_f = 0.6$
ℓ_{RVE} [constant radius]	80	85	75	60
ℓ_{RVE} $[r \sim \mathcal{N}(\bar{r}, 0.1\bar{r})]$	95	90	90	70

Table 1: Estimation of ℓ_{RVE} for different V_f values

	Gebart (hexa.)	Gebart (quad.)	Bodaghi et al. (2016)	Yazdchi et al. (2012)
$\bar{\varepsilon}$ (%)	78.4	39.9	19.4	14.4

Table 2: Mean relative difference w.r.t. mean permeability values

V_f	0.3	0.4	0.5	0.6
C_k (%)	2.6	2.6	3.0	2.9

Table 3: Coefficient of variability of permeability for different V_f values

V_f	0.3	0.4	0.5	0.6
$\bar{\varepsilon}$ (%)	0.75	1.2	0.91	1.3

Table 4: Mean relative difference between data mean values and sigmoid model

	No-slip	$\ell_s = 6$ nm	$\ell_s = 10$ nm	$\ell_s = 1$ μm	$\ell_s = 100$ μm	Free-slip
95% of permeability distribution ($\times 10^{-14}$ m^2)	[3.15 , 3.55]	[3.24 , 3.65]	[3.30 , 3.71]	[12.3 , 13.8]	[27.8 , 31.2]	[28.2 , 31.7]
Relative difference between $\bar{k}$ and mean value (%)	-	2.7	4.5	∼300	>700	>700

Table 5: Mean permeability (no-slip and realistic slip length)